JOURNAL OF PROPULSION AND POWER
Vol. 14, No. 5, September–October 1998

High-Power Hydrogen Arcjet Thrusters

Monika Auweter-Kurtz,* Thomas Gölz,† Harald Habiger,‡ Frank Hammer,†
Helmut Kurtz,† Martin Riehle,§ and Christian Sleziona¶
University of Stuttgart, Stuttgart D-70550, Germany

A radiation-cooled thermal arcjet thruster named HIPARC-R has been developed and investigated. It has been designed for the 100-kW power level and is operated with hydrogen as its propellant. A specific impulse of 1970 s was obtained with a mass flow rate of 150 mg/s at the 100-kW power level and at a thruster efficiency of about 28%. This equals a specific input power value of 670 MJ/kg. Parallel to the experiments a numerical code system was developed to further optimize the next generation of hydrogen arcjet thrusters. This code system consists of a finite volume flow code coupled with program modules for the calculation of thermal, chemical, and electronical properties. In addition, a program module for the calculation of the heat flow inside the thruster, including heat exchange, has been applied to model the heat transfer processes during thruster operation. The thruster has been operated over a wide power range and has been intensively investigated for the qualification of the numerical code system. Within this paper the experimental setup and the code system are described, the performance data are presented, and experimental and numerical results are compared.

Nomenclature

B = magnetic field
D = diffusion coefficient
E = electric field
e = charge of electron
$\hat{e}$ = specific energy
H = specific enthalpy
$\mathbb{1}$ = unit matrix
j = current density
k = Boltzmann constant
M = molecular mass
n = number density
p = pressure
q = heat flux
r = radial coordinate
T = temperature
t = time
v = velocity
z = axial coordinate
α = coupling coefficient
δ = deviation
ε = energy
η = efficiency
λ = thermal conductivity
ρ = density
σ = electric conductivity
τ = relaxation time
$\mathbb{T}$ = stress tensor
ψ = mole fraction
ω = chemical source term

Subscripts

e = electron
eff = effective
h = heavy particle
H_2 = hydrogen molecule
ion = ionization
pl = plasma
react = reaction
v, vib = vibrational
ν = species

Received Sept. 2, 1997; revision received Jan. 30, 1998; accepted for publication Feb. 6, 1998.

*Prof. Dr.-Ing. habil., Institut für Raumfahrtsysteme, Pfaffenwaldring 31. E-mail: auweter@irs.uni-stuttgart.de. Member AIAA.
†Dipl.-Ing., Institut für Raumfahrtsysteme.
‡Dr.-Ing., Institut für Raumfahrtsysteme. Member AIAA.
§Dipl.-Ing., Institut für Raumfahrtsysteme. Member AIAA.
¶Dr.-Ing., Institut für Raumfahrtsysteme.

Introduction

THERMAL arcjet thrusters at low-power levels have been in use on spacecraft for several years for north–south stationkeeping (NSSK) and will be deployed for primary propulsion on the P3D radio amateur satellite in 1998.[1,2] A U.S. Air Force space demonstration, ESEX, will fly a 26-kW arcjet thruster.[3] Future applications of medium-power arcjets may include orbit raising, repositioning, maneuvering, and drag compensation of large satellites and space stations.

These initial arcjet deployments use easily storable propellants such as ammonia and hydrazine. The best specific impulse and efficiency data with these propellants are relatively modest, <800 s and 40%, respectively. Superior results can be achieved with hydrogen: Hydrogen has an excellent specific heat capacity, which leads to better heat absorption of the propellant and, hence, the possibility of using regenerative heat transfer. Because the effective nozzle exit velocity is approximately proportional to the reciprocal value of the square root of the molecular mass, the theoretical highest specific impulse can also be expected. A disadvantage of hydrogen is the issue of storability; this is particularly important for long-duration missions, which has not yet been satisfactorily solved. However, many future space missions like platforms and stations will have substantial quantities of hydrogen onboard. In these applications the boil-off from cryogenically stored hydrogen, which otherwise has to be dumped into space, could be used for propulsion purposes. Therefore, a new emphasis in the development of hydrogen arcjets has appeared in the last few years.

For manned interplanetary missions, to Mars for example, high specific impulse at high thrust levels is required. Therefore, high-power thrusters are under consideration for this purpose. High power in the range of some megawatts will be necessary for the mission to the planet, which can be partially used for propulsion purposes during the cruise phase. Solar as well as nuclear thermal thrusters have been investigated for

this purpose. The only propellant candidate for both thruster types is hydrogen, and both are restricted to specific impulses below 800 s. If hydrogen is ensured to be a propellant candidate, much higher specific impulses can be achieved with hydrogen arcjets. In case the storage problem with hydrogen cannot be satisfactorily solved for interplanetary missions in the near future, high-power arcjets will be able to be operated with ammonia. In this case, 800-s specific impulse can be expected, but with significant savings in the propellant storage mass compared with solar and nuclear thermal thrusters. Therefore, the development of high-power arcjets in the 100-kW range was initiated in 1988. The program was largely experimental with supporting analytical and numerical work providing guidance.

At that time the knowledge and experience with high-power arcjets was mostly limited to the 30-kW level.[4] Russian publications were not available at that time. Therefore, as a first step a water-cooled arcjet was built to study the thruster behavior at the 100-kW power level.[5] A modular design was chosen for the investigation of the anode arc attachment; the heat flux distribution in the nozzle; and the optimization of the cathode position, propellant, injection, and nozzle throat diameter (Fig. 1). The water-cooled high power arcjet thruster HIPARC consisted of a stack of four individually water-cooled anode segments, which together formed a conical nozzle with a half-angle of 20 deg. The current input could be measured individually for every anode segment. The nozzle throat diameter could be varied from 2.5 to 6 mm by changing the constrictor segment. The data shown in this paper are those with the 4-mm nozzle throat. The injection angle of the propellant into the arc chamber could be changed through different inserts. This work showed that at this power level tangential injection for a swirl stabilization of the arc has no influence on the thruster performance and behavior. With this thruster and the 6-mm-diam constrictor, a maximum input power of 140 kW could be achieved, and the best performance in operation was observed at a mass flow rate of 200 mg/s and an input power of 100 kW. A thrust value of 3 N led to a specific impulse of 1500 s at a thrust efficiency of 22%.[6] Based on the experience gained with the water-cooled thruster, a radiation-cooled 100-kW arcjet device named HIPARC-R was designed, built, and investigated (Fig. 2). The experimental setup including thruster design, thrust balance, and the test facilities are described in the second section; the performance data are presented and discussed in the third section.

The numerical code system developed for further optimization of the next thruster generation is based on two codes that were developed for self-field magnetoplasmadynamic (MPD) thrusters and low-power arcjets. For the simulation of the plasma flow within the arcjet thruster, the code developed at the same institute for the simulation of self-field MPD thrusters with argon as the propellant was chosen as the baseline.[7] It is a finite volume code consisting of different modules for the flowfield including the nonequilibrium chemistry, electrical current density, and electron temperature that are iteratively solved. This code has been modified for hydrogen as

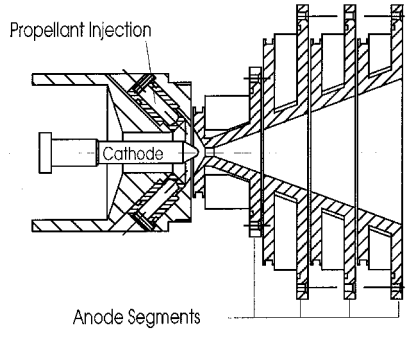

Fig. 1 Water-cooled HIPARC thruster.

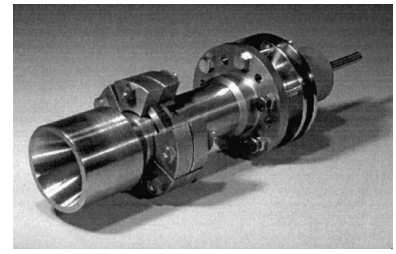

Fig. 2 Radiation-cooled HIPARC-R thruster.

the propellant and with respect to the much higher pressure situation compared to MPD devices. For the thermal analysis of the thruster in the transient and stationary operation phases of the thruster, a finite element program system has been used. This code has already been applied successfully for the optimization of low- and medium-power arcjets.[8,9] In the fourth section of this paper both code systems are described and numerical results are presented and discussed with respect to the performance measurements and thermal thruster behavior.

To further qualify the numerical code the arcjet plume has been investigated experimentally. The methods applied are described and experimental and numerical results are presented and compared in the fifth section.

Experimental Setup

Thruster

HIPARC-R is a constrictor-type thermal arcjet with a conical nozzle at a half-angle of 20 deg (Fig. 3). The nozzle dimensioning of HIPARC-R was based on thermal efficiency measurement data obtained with the water-cooled device (Fig. 1),[5,6] data obtained with the 10-kW class thermal arcjet thrusters,[10,11] and data published by Sankovic and Curran.[12] The design of the cathode, nozzle, and arc chamber is similar to the water-cooled device but with a nozzle throat diameter of 4 mm, a constrictor length-to-diameter ratio of 1, and an area ratio of 1:225 compared with 1:256 in the case of the water-cooled thruster. The converging part of the nozzle offers a 50-deg opening half-angle. The 10-mm-diam cathode is mounted on the gas-supply tube in the thruster's centerline. This diameter proved to be best suited for this power level with the water-cooled device.[5] The cathode tip is conical with a half-angle of 30 deg.

The thruster was designed as a laboratory device with the vital parts being easily changed with respect to further optimization. Therefore, the HIPARC-R consists of a nozzle corpus that is fixed to the thruster housing by six pairs of TZM, a molybdenum alloy, brackets (Figs. 2 and 3).

The thruster sealing is done by graphite foil rings 0.35 mm thick. The sealing pressure force is supplied by the TZM brackets between the nozzle and the housing, by steel disks on the back side, and by a spring made of Haynes alloy 230® inside the thruster. Cathode and anode are electrically isolated by parts made of boron nitride and a glass ceramic material, respectively.

The propellant gas is fed by a stainless-steel tube at the thruster center. It is used as current supply and as cathode fixation. The gas is hereby used as the current supply cooling medium. It exits the tube near the spring and is led to a channel between the thruster housing and main insulator, where it is heated regeneratively. Farther downstream it is injected into the arc chamber through four bore holes (each 0.75 mm in diameter), directing axially to the cathode tip. A swirl is not induced based on the results of the injection optimization with the water-cooled device.[6]

The arc chamber pressure in the propellant injection region can be measured during thruster operation. A TZM tube is screwed to the thruster housing leading to a pressure tap.[13] This tube is water-cooled by a cooling sleeve at a distance of 30-cm off the thruster.

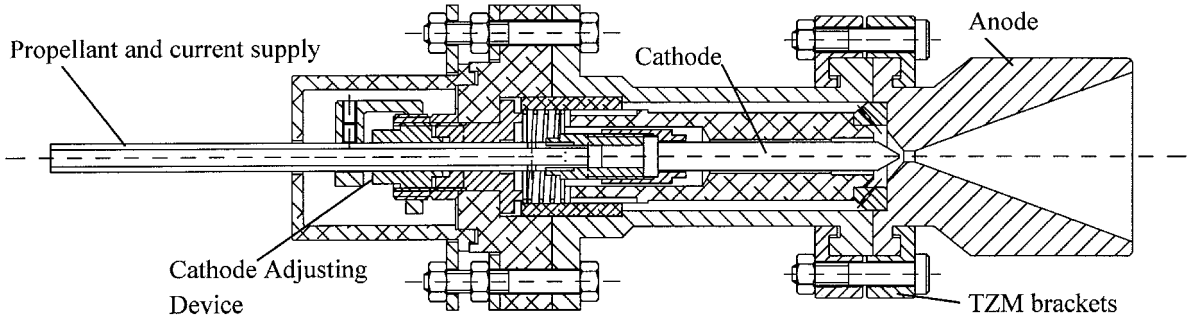

Fig. 3 Schematic drawing of HIPARC-R thruster.

The cathode gap can be adjusted by a mechanism that allows adjustment before sealing the cathode tube feedthrough. This adjustment device is covered by a ceramic cap to prevent arc-overs to the thruster parts at anode potential.

Thrust Balance

The HIPARC-R thruster is mounted on the same thrust balance that was used for its water-cooled predecessor HIPARC, which is an improved version of the parallelogram-type balance used at the Institut für Raumfahrtsysteme (IRS) for all high-power thrusters.[14] The movable part of the balance carrying the thruster is suspended on three swing arms, each supported by two knife-edge bearings. The thrust force is transmitted as a tension force by a thin wire over a reversing pulley to a water-cooled measuring box that contains the force transducer. To allow the calibration of the balance under vacuum conditions, a remotely operated weight lever has been installed. This lever places a weight on a scale that creates a defined force on the platform. The electric power is fed to the thruster via two copper rods submerged in mercury-filled tubes. To avoid evaporation of the mercury, its surface is sealed with silicon oil. The cooling water for the thrust balance interface and the thrust balance structure is fed to the platform by semicircular hoses allowing minimum stiffness. Effects of stiffness and friction are calibrated for each measuring sequence before ignition and checked after engine shutdown under vacuum conditions.

Test Facilities

The HIPARC-R thruster and the thrust balance are integrated in a stainless-steel tank 4.5 m long and 2 m in diameter. This vacuum chamber is double walled to provide water cooling of the tank during thruster operation.

Three mass flow controllers calibrated for hydrogen have been integrated into the IRS gas-supply system, enabling a wide range of propellant gas flows to be tested. The mass flow controller readout is checked by weight balancing of the gas bottles with an accuracy of ± 1 g.

The power is supplied by a current-regulated thyristor rectifier consisting of six identical units each capable of supplying 1 MW. These may be connected in series or parallel, thus varying the desired output level of current (maximum 48 kA), voltage (maximum 6 kV), and power (maximum 6 MW). The ripple of the current is less than 0.5%.

The pumping system is a four-stage roots pump system; the total suction power amounts to 250,000 m^3/h at 10 Pa, which is sufficient for high-power arcjet testing.

Performance Data

The voltage–current characteristics of the water- and radiation-cooled thrusters are compared in Fig. 4. The higher power level in the case of HIPARC-R indicates that the anode attachment is located farther downstream in the nozzle compared with the water-cooled device. Therefore, the power input is also increased at a given current level. The voltage is nearly constant over a wide range of power in the case of HIPARC-R, which is a sign of a high ionization level. In Fig. 5 the measured thrust is plotted against the input power for different mass flow rates. A maximum thrust of 4.0 N was achieved for the maximum mass flow examined (300 mg/s H_2) at a power level of 100 kW. The best result in terms of specific impulse was achieved with the minimum mass flow rate being examined (150 mg/s H_2), for which the thruster still works in a stable mode. A specific impulse of 1970 s could be achieved at 100-kW power input, which corresponds to 670-MJ/kg specific input power. Figure 6 clearly shows that specific input power as well as specific impulse values are highest for the lowest investigated mass flow rate.

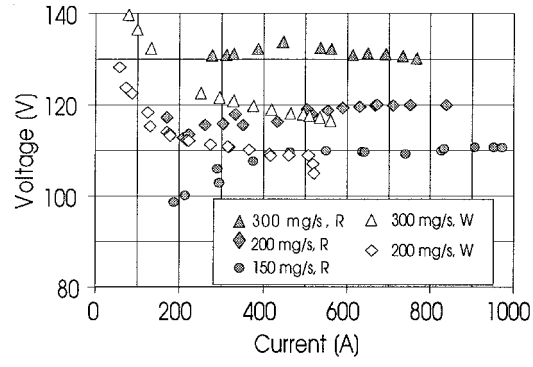

Fig. 4 Voltage/current diagram for the radiation-cooled (R) and the water-cooled thruster (W).

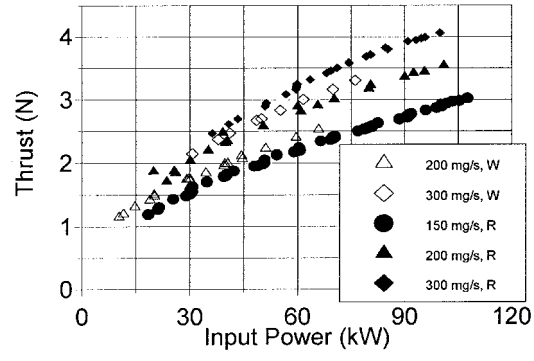

Fig. 5 Thrust vs input power for the radiation-cooled (R) and the water-cooled (W) thruster.

In the case of the radiation-cooled thruster, the thrust efficiency values for this device lie in the range of 25–30% (Fig. 7). The thrust efficiency is defined as beam power related to the electrical input power.

At a given power setting the arc chamber pressure is significantly higher with the radiation-cooled device than with the water-cooled thruster.[15] At a power level of 60 kW with a 300 mg/s mass flow rate, 100 kPa were measured in the case of the water-cooled device and 130 kPa with HIPARC-R. This indicates a higher average temperature and, thus, a higher pro-

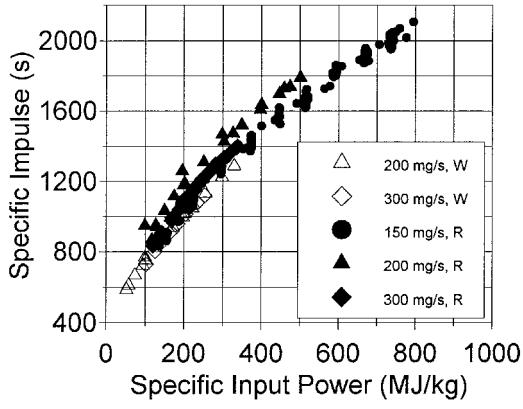

Fig. 6 Specific impulse vs specific input power for the radiation-cooled (R) and the water-cooled (W) thruster

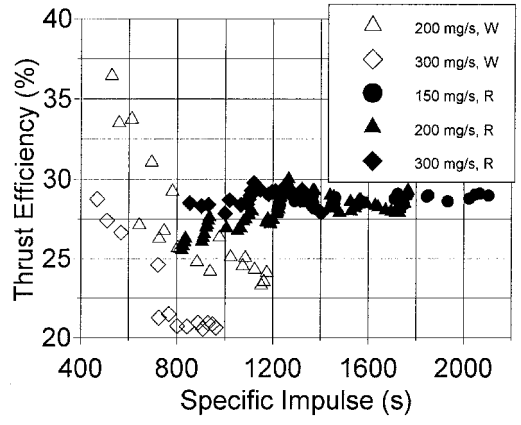

Fig. 7 Thrust efficiency vs specific impulse for the radiation-cooled (R) and the water-cooled (W) thruster.

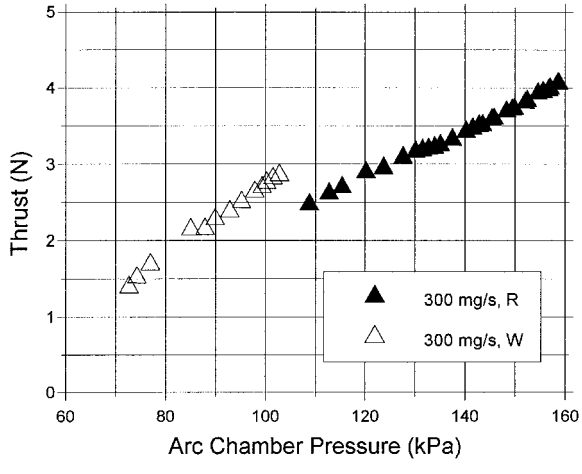

Fig. 8 Thrust vs arc chamber pressure for the radiation-cooled (R) and the water-cooled (W) thruster.

pellant gas enthalpy in the arc chamber because of the regenerative cooling of the thruster housing.

At the same time, the thrust vs arc chamber pressure characteristic is nearly linear, with different slopes, for the water- and radiation-cooled thruster versions (Fig. 8). The steeper slope yields higher thrust values with the water-cooled device at the same value of the arc chamber pressure than with the radiation-cooled device. This is because of the higher mass flow rate with the water-cooled thruster at the same chamber pressure. The HIPARC thruster design is not a preflight design but rather a laboratory model, and no life tests have been performed. The accumulated running time was approximately 50 h at the end of 1996 and no damage at the anode was noticed.

Numerical Thruster Analysis

Two code systems have been developed to improve the understanding of the thermal arcjet behavior and to further optimize the device.

Plasma Flow Analysis

A numerical code system describes the plasma flow through the HIPARC-R thruster, including electrode effects. Because of the existence of thermal nonequilibrium, three different temperatures are taken into account: 1) The electron temperature T_e, 2) the vibrational temperature T_v, and 3) the translational temperature T of the heavy particles. For the chemical reaction model nonequilibrium effects must also be considered. The transport coefficients are calculated with the Yos model.[16] The code has a modular construction and consists of separate modules for the flowfield including the chemical reactions and the vibrational energy balances, electrical discharge equations and the electron energy balances. The modules are called up subsequently and the solution is found by an iteration process. The solution is produced with the help of a numerical grid that is formed so that the contour conforms to the shape of the grid with respect to the axial symmetry of the problem.

Flowfield

The flow calculation is performed by means of a modified code that has been used before for MPD calculation.[7] The basic equations for the calculations of the flowfield are the following Navier–Stokes type of conservation equations.

Mass equation:

$$\frac{\partial}{\partial t}\rho + \nabla(\rho\hat{\boldsymbol{v}}) = 0 \tag{1}$$

Momentum equation:

$$\frac{\partial}{\partial t}\rho\hat{\boldsymbol{v}} + \nabla\rho\hat{\boldsymbol{v}} \otimes \hat{\boldsymbol{v}} - \nabla(-p\mathbf{I} + \boldsymbol{\tau}) = \hat{\boldsymbol{j}} \times \hat{\boldsymbol{B}} \tag{2}$$

Energy equation for the heavy particles:

$$\frac{\partial}{\partial t}\hat{e}_h + \nabla(H)\hat{\boldsymbol{v}} - \nabla\boldsymbol{\tau} - \nabla\lambda\nabla T - \nabla\lambda_v\nabla T_v = \nabla\sum_{v=h} H_v D_v \nabla\psi_v + \hat{\boldsymbol{v}}(\hat{\boldsymbol{j}} \times \hat{\boldsymbol{B}}) + \sum_{v=h} n_v n_e \alpha_{ev}(T - T_e) \tag{3}$$

The coupling to the other energetical relevant effects is performed by source terms that are calculated in separate program modules.

Vibration Energy

The conservation equation of the vibrational energy can be written as

$$\frac{\partial}{\partial t}\hat{e}_v + \nabla\hat{e}_v\hat{\boldsymbol{v}} - \nabla\lambda_v\nabla T_v = \nabla\hat{e}_v D_{H_2}\nabla\psi_{H_2} + \omega_{H_2}\hat{D}_{H_2} + \frac{\hat{e}_v(T) - \hat{e}_v(T_v)}{\tau_{H_2}} + \frac{M_{H_2}}{M_e}\frac{\hat{e}_v(T_e) - \hat{e}_v(T_v)}{\tau_{e-H_2}} \tag{4}$$

Diffusion, dissociation, and ionization processes as well as energy exchange with the translation energy of the heavy particles and with electrons are taken into account on the right-hand side of the equation, where τ represents the relaxation times.

Electron Energy

In the case of stationary conditions and neglecting radiative losses, the electron energy equation can be written as

$$n_e\hat{\boldsymbol{v}}\cdot\nabla\left(\frac{3}{2}kT_e\right)+p_e(\nabla\cdot\hat{\boldsymbol{v}})+\frac{3}{2}\frac{k}{e}T_e(\nabla\cdot\hat{\boldsymbol{j}})+\frac{\hat{\boldsymbol{j}}}{en_e}\cdot\nabla p_e+\nabla\hat{\boldsymbol{q}}_e^*$$
$$=\sum_{\nu}n_\nu n_e\alpha_{e\nu}(T-T_e)-\varepsilon_{\text{ion}}\left.\frac{\partial n_e}{\partial t}\right|_{\text{react}}+\frac{|\hat{\boldsymbol{j}}|^2}{\sigma} \tag{5}$$

On the right side of Eq. (5) the energy transfer between the plasma components, the energy loss by ionization, and the Ohmic heating are considered. Here, ε_{ion} is the ionization energy of a hydrogen atom. The electron temperature as the solution of this equation is coupled into the other calculation modules. This module uses a finite difference scheme for the solution.

Electrical Discharge

Taking Maxwell's equations for an electrically neutral and stationary plasma and Ohm's law for a plasma flow the current density in the flowfield can be determined:

$$\hat{\boldsymbol{j}}=\sigma(\hat{\boldsymbol{E}}+\hat{\boldsymbol{v}}\times\hat{\boldsymbol{B}})-\frac{\sigma_e\tau_e}{B}(\hat{\boldsymbol{j}}\times\hat{\boldsymbol{B}}-\nabla p_e) \tag{6}$$

Chemical Reactions

Chemical processes inside a rocket engine can be classified by the time a particle has to interact with other particles. If the time is sufficiently long, the composition tends toward a chemical equilibrium composition; whereas when the gas velocities are sufficiently high, the reaction time is so short that almost no changes in compositions can be detected and the flow in this case has to be taken as frozen. Within a thermal arcjet thruster the plasma flow is in chemical equilibrium in the chamber and nozzle throat area, in nonequilibrium in the downstream expansion area close to the nozzle throat area, and is frozen downstream in the expansion nozzle. Therefore, for the calculation of the plasma flow within a thermal arcjet thruster, the finite rate chemistry approach has been applied that is based on the model of Scott.[17] The reaction rates are determined as functions of the different energy states, such as electron temperature, heavy particle translational, and vibrational temperature. Through the coupling with the velocity vector, the reaction time per grid cell can be calculated.

The species considered for this application are H_2, H, H^+, H_2^+, and e^-. For each of these species, a conservation equation must be solved to obtain the nonequilibrium chemical composition over the flowfield:

$$\frac{\partial}{\partial t}n_\nu+\nabla n_\nu\cdot\hat{\boldsymbol{v}}=\omega_\nu+\nabla n_\nu D_\nu\nabla\psi_\nu \tag{7}$$

n_ν is the particle density of the species ν; ω_ν is the chemical source term, which describes the change in particle density by the chemical reactions; D_ν is the diffusion coefficient; and ψ_ν is the mole fraction of species ν.

Boundary Conditions

As boundary conditions for the plasma flow calculation, the current and temperature distribution on both electrode surfaces are needed. These follow from a detailed electrode model based on the work of Ecker.[18] To determine the current distribution, thermal and field emission of electrons and the current transport by electrons and ions coming from the quasineutral arc column are taken into account for each grid cell on the electrode surfaces. The given total current is guaranteed to be reached by integrating over the electrode surface and, therefore, also provides us with the electrode voltage.

To determine the heat-flux distribution in addition to the charged particles, the neutral particles that leave the surfaces are also taken into account. Surface radiation with an emission coefficient of 0.42, which was close to a value used for similar applications,[19] as well as conductive heat transport from the plasma flow and the ohmic heating in the electrode are considered. The surface temperature distribution on the electrodes came from a simplified thermal calculation of the thruster body, where the heat transport within the electrodes is also regarded.

At the inflow boundary a simulation of a mass flux controller satisfies the mass flow rate with an adjustable pressure and a given temperature. This boundary condition represents an outflow from a variable reservoir into the calculation area. Therefore, the resulting pressure in the chamber behind the inflow boundary can be taken as a comparison with experimental values because no pressure input from the experiment is necessary to determine the inflow condition. The outflow boundary is considered to be a freestream boundary, and either the independent flow variables are completely extrapolated for the case of supersonic conditions or the pressure is given for the case of subsonic conditions. In the case of inflow conditions at the outflow boundary, an inflow from a reservoir at ambient condition is determined. The principle of reflection was applied for the symmetry axis. No flux condition is taken for the mass and momentum conservation equation at the electrode walls. The boundary condition at the walls for the heavy particle energy equation is determined from a calculated wall temperature; this follows from the electrode model.[18] This model considers all heat flux losses and gains. The electron temperature boundary condition is given by $\nabla T_e\cdot\boldsymbol{n}=0$, where $\boldsymbol{n}$ is the normal vector of the surfaces. Because of the axial symmetry, $(\partial T_e/\partial r)=0$ can be assumed to be on the axis.

Numerical Results

The results presented here were gained for the 70-kW test case at a mass flow rate of 200 mg/s. The desired power level was achieved in the experiment for a current setting of 583 A. The voltage adjusted itself at 120 V and a thrust of 2.81 N was measured that corresponds to an effective exhaust velocity of 14.1 km/s. For the flowfield calculation the mass flow rate and the current setting were taken from the experiment. In addition, the temperature of the propellant inflow had been estimated to be 800°C in accordance with previous thermal analysis results.

The current and velocity distributions within the HIPARC-R thruster are shown in Figs. 9 and 10, respectively. Figure 11 shows a more detailed distribution of the velocity at the nozzle exit plane.

Because of the moderate power level the anode attachment region is located near the nozzle throat. The discharge voltage was calculated with 113 V, 29 V of it was a result of electrode falls. The total thrust level and the effective exhaust velocity can be inferred from the velocity and mass flow distribution at the nozzle end, yielding a thrust of 4.1 N and an effective

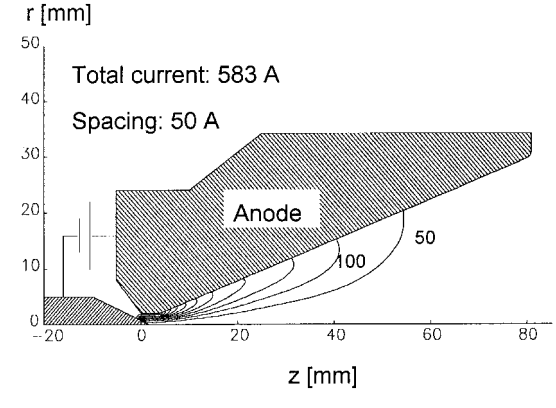

Fig. 9 Current distribution within HIPARC-R.

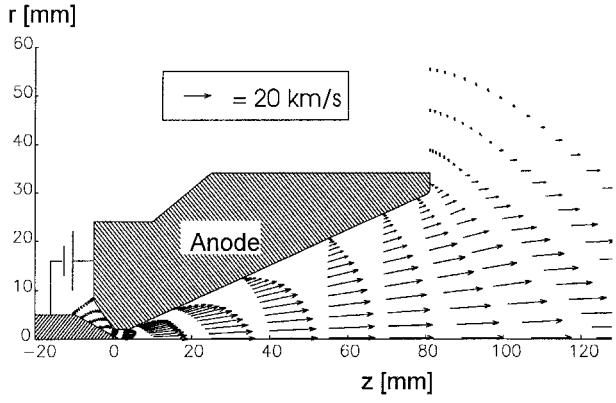

Fig. 10 Velocity distribution within HIPARC-R.

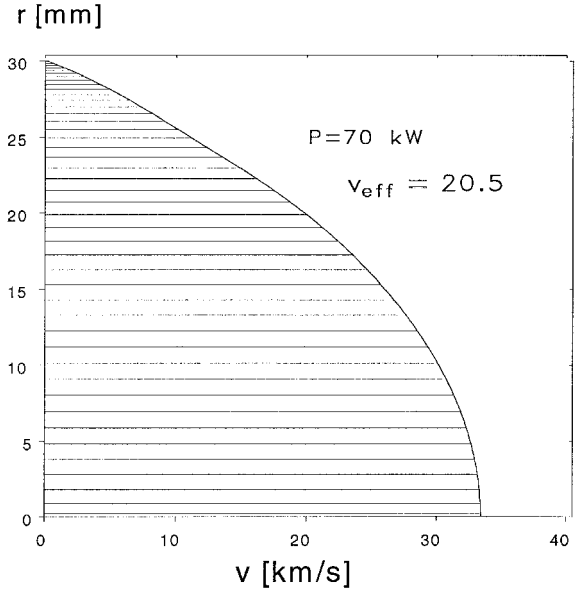

Fig. 11 Velocity distribution at the nozzle exit of HIPARC-R.

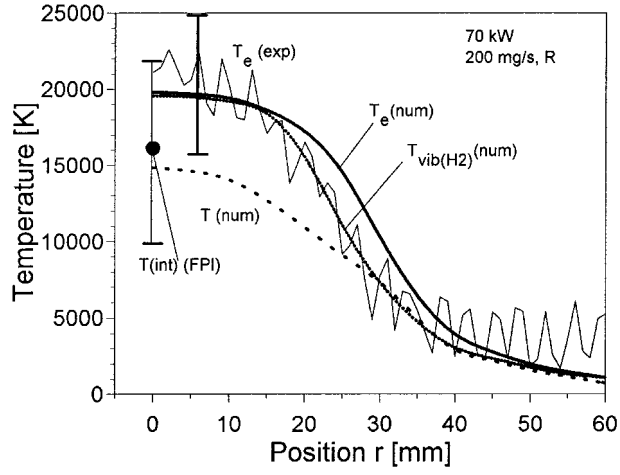

Fig. 12 Experimental and numerical temperature profiles 50 mm to the nozzle exit.

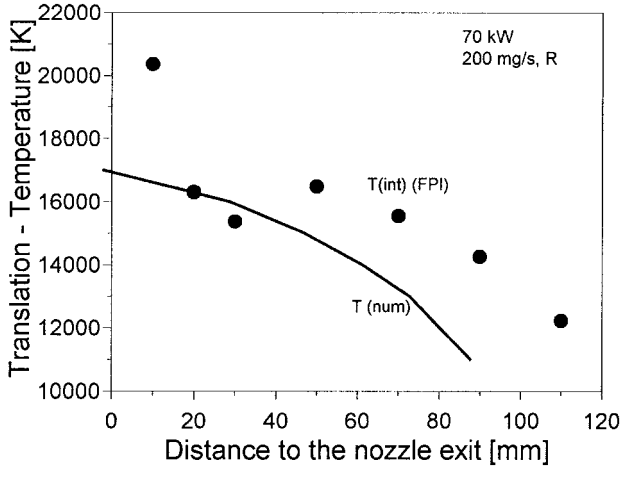

Fig. 13 Integrated experimental and local theoretical values of the translation temperature on the plasma jet centerline.

exhaust velocity of 20.5 km/s. The measured thrust value is 31% lower compared with the calculated one. There are two main reasons for this discrepancy. Firstly, the calculated chamber pressure was 156 kPa. This value is higher than determined in the experiments. As can be seen from Fig. 9, a chamber pressure value of about 160 kPa was reached in the 300-mg/s mass flow rate case at the 100-kW power level, resulting in a thrust level of 4.1 N. For the 70-kW case no pressure measurements are available but the expected value is certainly lower. Secondly, the high thrust could be caused by the nonequilibrium chemistry model that was used.[17] This model was originally designed for microwave plasma sources that operate at a much lower temperature level. The recombination rates for the dissociation might be too high. This could be converted to kinetic energy and accelerate the heavy particles more than during actual operation. This would also explain the lower calculated translational temperature that is obvious from Figs. 12 and 13.

The calculated temperature distribution of the electron, vibration, and translation temperatures are shown in Fig. 14.

Within the plasma core, electron and vibration temperatures are very close together; they only differ significantly in the boundary layer of the thruster and at the flow boundary, which is also obvious from Fig. 12, where the temperature profiles are plotted 50 mm from the nozzle exit plane. The translational temperature is significantly lower within the thruster because of the frozen flow effect.

The concentrations of hydrogen molecules, atoms, and ions with respect to the heavy particles are shown in Fig. 15.

The concentration of the ionized hydrogen atoms is almost equal to the electron density because H_2^+ is almost lower than 1/100 H^+. For this quantity, the agreement between measured and calculated values is good as can be seen from Fig. 16, where the density profile is plotted 50 mm from the nozzle exit. It is obvious from Fig. 15 that the propellant is fully dissociated within the thruster and fully ionized within a large region.

Thermal Analysis

For the optimization of the thermal behavior of arcjet thrusters, a numerical code had been developed that allows detailed investigation of the transient stage after ignition up to the steady-state operation of these devices.[8,9] Heat conduction along the structure, radiation interchange between thruster components in the hot region of the thruster, radiative cooling of the body, as well as radiative heating of the propellant flow have been taken into account. The temperature dependence of the material properties has to be considered properly. The internal propellant flow is considered as a laminar Navier–Stokes flow that is thermally coupled to the thruster body. To reduce the calculation time, the geometry was reduced to two-dimensional axial symmetry with balanced volumes and surfaces for the simplified parts. The finite model that was used for this investigation contained more than 4500 nodes for the description of the structure and the flowfield. A decisive and sensitive point is the way the contact planes are modeled in such a laboratory thruster. A variety of calculations have already been performed with low- and medium-power arcjet

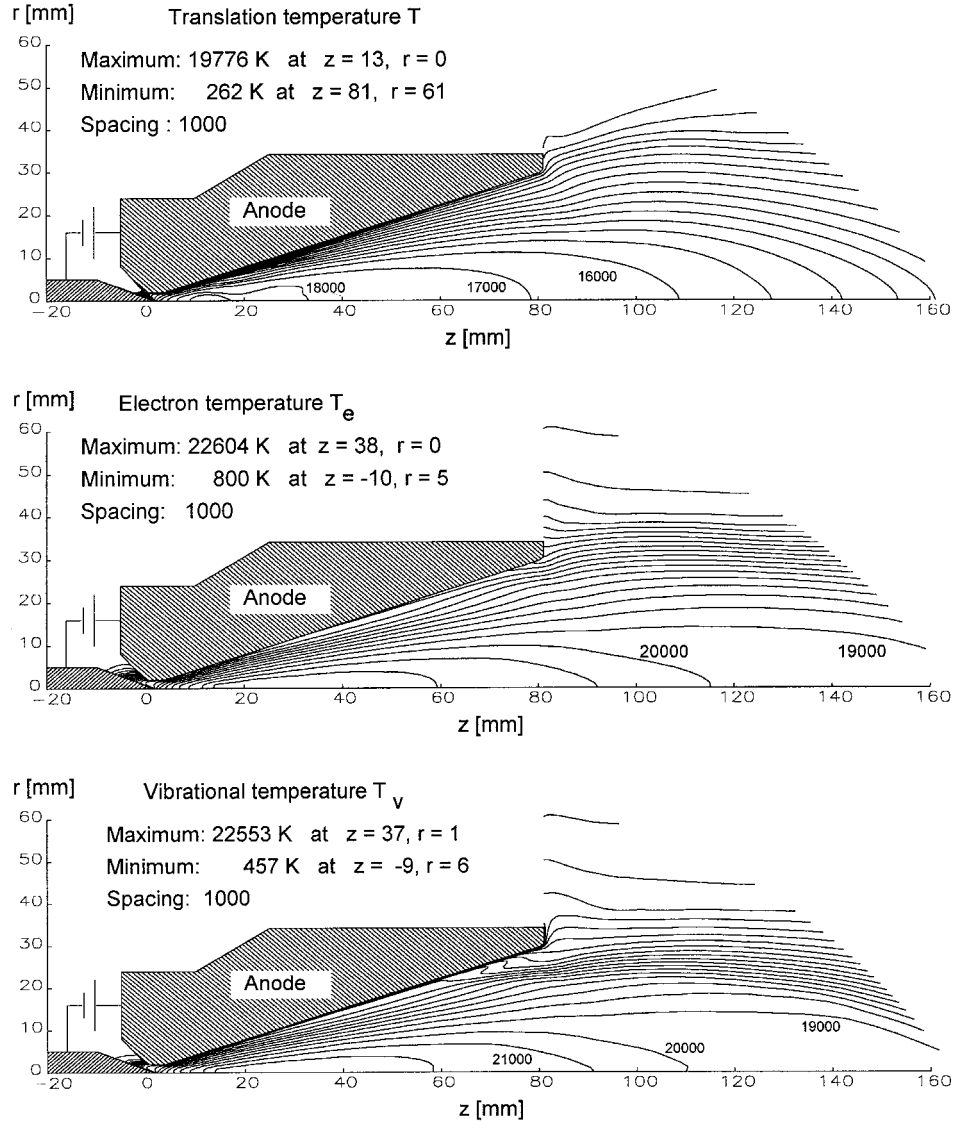

Fig. 14 Translational, electron, and vibrational temperature distribution within HIPARC-R.

thrusters to determine these contact plane resistances by comparing the numerical results with the experimental data.

The heat-load distribution to the thruster has been derived from the results with the water-cooled device. With the radiation-cooled HIPARC-R the temperature distribution of the tungsten anode has been observed using a thermal camera. The total heat load of the thruster has been determined by varying this quantity and comparing the numerical and experimental results. From Fig. 17 the total heat load of about 5.0 kW at stationary conditions for the investigated power level (700 kW) and mass flow (200 mg/s) can be derived. For this value an excellent agreement between measured and calculated temperature distribution is obtained. Furthermore, a strong dependency of the temperature level as a function of total heat load is obvious from Fig. 17.

Figure 18 shows the calculated thermal behavior of the thruster during the heat-up phase after ignition for the same test case. The large temperature gradients at certain joints of different thruster parts can be clearly seen. The maximum temperature with values of about 2100°C are reached at the arc attachment area at the anode. Because of the good thermal conductivity of the tungsten material, the outer surface temperature still reaches 2000°C. At this surface and temperature level, the major part of the heat is radiated off at an estimated emissivity of $\varepsilon = 0.5$ for the uncoated but roughly machined surface quality of the tungsten body. The emissivity was obtained by simultaneously measuring the surface temperature using the thermocouples and a pyrometer.

Plume Investigation

The plasma plume measurements were performed with electrostatic probes and Fabry–Perot interferometry (FPI). Electron temperatures and electron densities of the arcjet plume were obtained by cylindrical electrostatic triple-probes.[20–22] With this type of probe the radial distribution of the electron temperature and the electron density can be measured by a fast radial motion of the probe through the investigated plasma flow. The probes are aligned with the plasma flow and designed to operate in the collisionless thin plasma sheath regime. The triple-probe consists of three symmetrical electrodes of equal surface areas, two of them connected as a double probe and a third floating with respect to the plasma. For an externally applied fixed potential difference in the double-probe circuit, an electron temperature-dependent potential difference can be measured between the double probe and the floating electrode. Therefore, by moving the probe through the plasma, direct radial and axial distributions of T_e can be obtained. From the collisionless probe theory and the current measured in the double-probe circuit, the electron number density can be calculated.

Translational temperatures of the heavy particles are measured by means of an FPI, which is used as a very high-res-

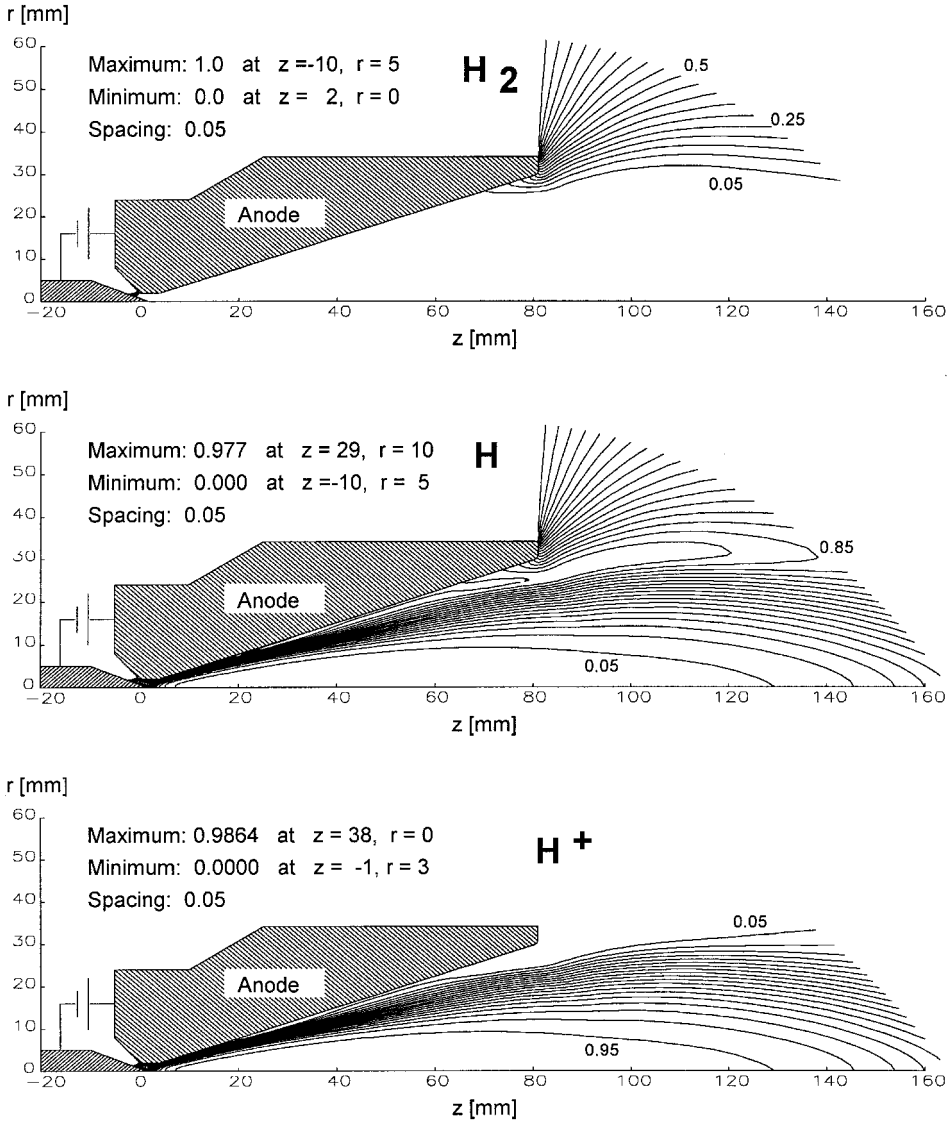

Fig. 15 Species concentrations of hydrogen molecules (H_2), atoms (H), and ions (H^+) with respect to the heavy particles.

olution emission spectroscope to measure the spectral line width of the Doppler-broadened H_α line. The Doppler linewidth of the emission-line profile is a function of the translational temperature, the known unshifted wavelength of the emitting spectral line, and the mass of the emitting particle.[23] The translational temperature is evaluated from a line of sight (LOS) measurement through the plasma jet. An Abel inversion was not possible because the Doppler linewidth of the emission line could not be resolved in the outer region of the plasma jet.

In Fig. 12, the experimental and theoretical temperature data are compared at a cross section 50 mm to the nozzle exit plane for a power level of 70 kW with a mass flow rate of 200 mg/s. The error bar related to the experimental triple-probe data shows the standard deviation of five measurements. The electron temperature measured with triple probes and the numeric calculations are in good agreement. The translation temperature measured with FPI on the plasma jet centerline is about 1200°C higher than the theoretical temperature, but it must be taken into consideration that the measured values are integrated values along the LOS through the plasma jet. This also applies to the measured temperatures shown in Fig. 13, which show the axial profile of the translational temperature in the plasma jet. With respect to the uncertainties of the measurement method (±40% of the measured value as shown by the error bar in Fig. 12), the agreement is good. The uncertainty is caused by the rather low intensities of the observed H_α line and the temperature evaluation process, considered by the Gaussian error propagation method. The lower calculated translational temperature might be caused by the chemical model applied as discussed in the fourth section of this paper. The measured and calculated electron densities show good agreement (Fig. 16).

Plasma velocities are measured with an electrostatic time of flight probe. For this purpose two electrostatic double probes separated at a known distance are positioned in the flow direction. Upstream and downstream probes are biased to draw ion-saturation current. Fluctuations in the local ion number density around a probe result in fluctuations in the detected ion current to the probe. By moving with the flow velocity v_{pl}, those fluctuations are first detected at the upstream probe and then time delayed at the downstream probe. By performing a fast Fourier transform cross-correlation with the two signals, the exact value of the time shift or rather the time of flight is easily determined. With a probe distance of 25 or 50 mm, the velocity of the plasma particles can be calculated. In Fig. 19 mean values of the measured plasma velocity at a cross section of 50 mm to the nozzle exit plane is plotted for the case of 30-kW power at 200-mg/s mass flow rate. Again, the error bars show standard deviations of five measurements. In comparison the theoretical plasma velocity at the same cross section for 70-kW power is shown. Because the 30-kW velocity

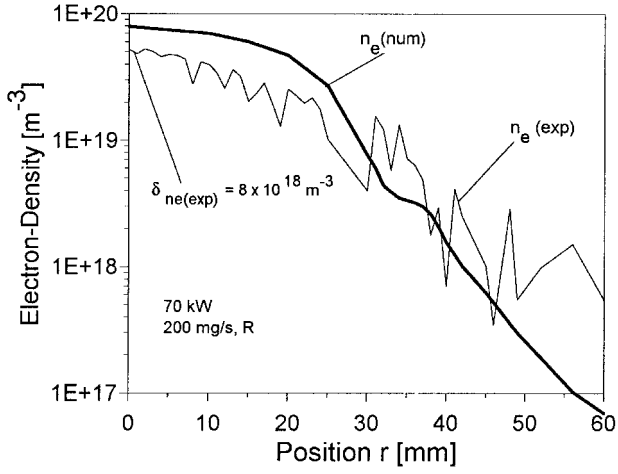

Fig. 16 Experimental and numerical electron density profiles 50 mm to the nozzle exit.

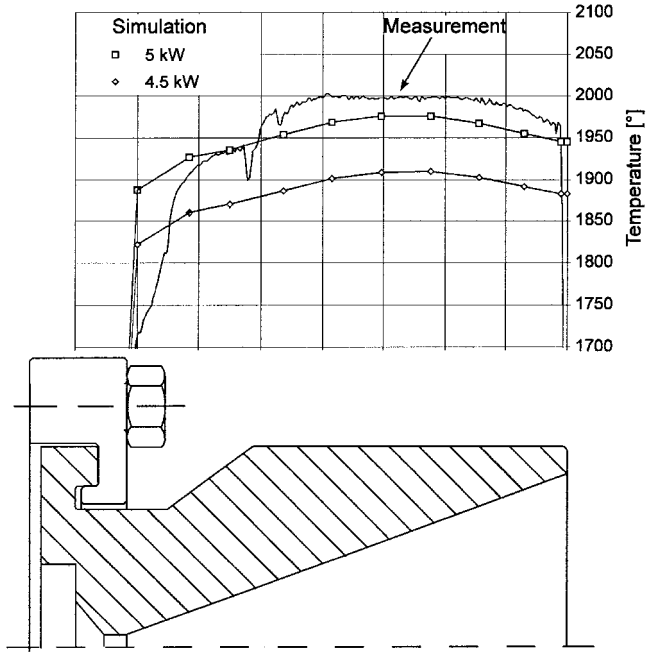

Fig. 17 Measured and calculated outer surface temperature distribution of HIPARC-R.

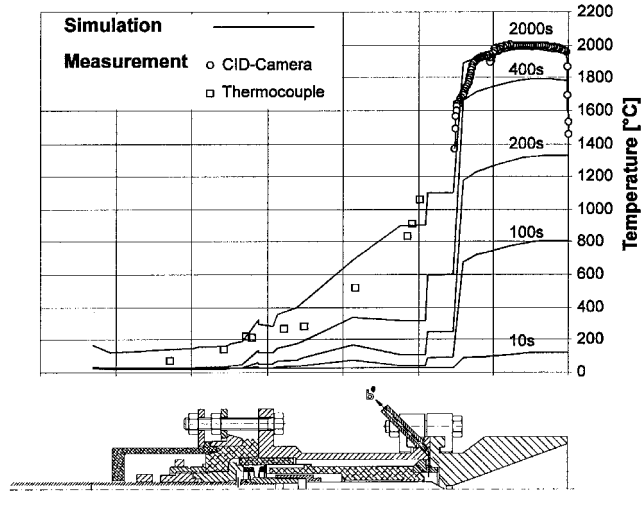

Fig. 18 Calculated surface temperature distribution as a function of time during ignition under stationary conditions compared with measured temperatures under stationary conditions.

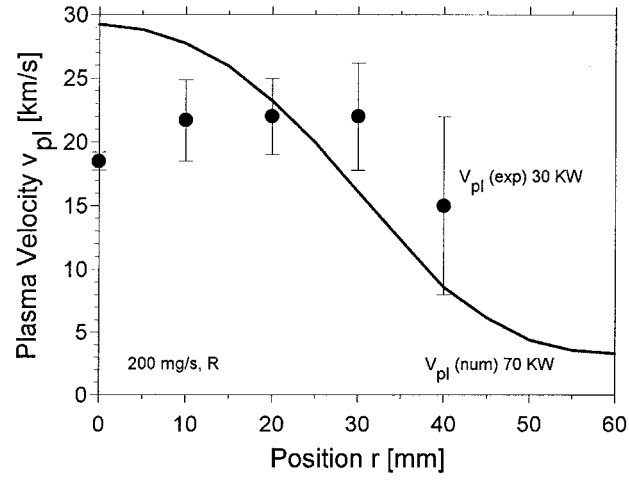

Fig. 19 Plasma velocity 50 mm to the nozzle exit measured with time of flight probes.

profile seems to be more flat than in the theoretical 70-kW case, the measured velocity drop on the plasma jet centerline requires further investigations together with measurements at a power level of 70 kW.

Conclusions

It is shown that a 100-kW thermal arcjet can be operated steady state in a high specific impulse mode. Specific impulse values of more than 2000 s at a thruster efficiency of 29% have been achieved with a nonoptimized laboratory model at a specific power level of about 800 MJ/kg. The thermal load to the thruster nozzle currently limits the thruster performance. The experimental and theoretical investigations of the radiation-cooled arcjet HIPARC-R can be used in the future to design and build an arcjet thruster with a regeneratively cooled anode. By optimizing the regenerative cooling capacity of this thruster the thruster efficiency can be increased as in the case of low- and medium-power devices. If it is also possible to operate the device at an increased specific power level, which is the most important design goal, a further increase of specific impulse can be achieved. Improvement of the regenerative cooling and a high-emissivity coating will hopefully aid in meeting this goal. The flow code and the thermal code can be used advantageously for this optimized design. Both have been qualified with the help of performance measurements, experimental and thermal analysis, and plume investigations. Further experimental and numerical investigations are needed to clarify the discrepancies in chamber pressure and thrust level.

References

[1]Anon., "Electric Propulsion," *Aerospace America*, Vol. 32, No. 12, 1994, p. 58.

[2]Messerschmid, E. W., Zube, D. M., Meinzer, K., and Kurtz, H. L., "Arcjet Development for Amateur Radio Satellite," *Journal of Spacecraft and Rockets*, Vol. 33, No. 1, 1996, pp. 86–91.

[3]Sutton, A. M., Bromaghim, D. R., and Johnson, L. K., "Electric Propulsion Space Experiment (ESEX) Flight Qualification and Operations," AIAA Paper 95-2503, July 1995.

[4]AVCO, "Thirty Kilowatt Plasma Jet Rocket Engine Development, Third Year Development Program," NASA LR-94079, RAD-TR-64-42, 1964.

[5]Gölz, T., Auweter-Kurtz, M., Kurtz, H. L., and Schrade, H. O., "High Power Arcjet Thruster Experiments," International Electric Propulsion Conf., IEPC Paper 91-072, Oct. 1991.

[6]Gölz, T., Auweter-Kurtz, M., and Kurtz, H. L., "100 kW Hydrogen Arcjet Thruster Experiments," AIAA Paper 92-3836, July 1992.

[7]Sleziona, P. C., Auweter-Kurtz, M., and Schrade, H. O., "Numerical Model for an MPD Thruster Calculation," *Computational Fluid Dynamics '94*, Wiley, New York, 1994, pp. 790–795.

[8]Viertel, Y. E., Schmitz, H.-D., Riehle, M., Kurtz, H. L., and Auweter-Kurtz, M., ''Development and Test of a 1 kW Hydrazine Arcjet System,'' AIAA Paper 96-2960, July 1996.

[9]Riehle, M., Habiger, H., Kurtz, H. L., and Auweter-Kurtz, M., ''Thermal Analysis and Optimization of Advanced Medium Power Arcjets,'' AIAA Paper 96-2701, July 1996.

[10]Glocker, B., Auweter-Kurtz, M., Gölz, T., Kurtz, H. L., and Schrade, H. O., ''Medium Power Arcjet Thruster Experiments,'' AIAA Paper 90-2531, July 1990.

[11]Glocker, B., and Auweter-Kurtz, M., ''Numerical and Experimental Constrictor Analysis of a 10 kW Thermal Arcjet,'' AIAA Paper 92-3835, July 1992.

[12]Sankovic, J. M., and Curran, F. M., ''Arcjet Thermal Characteristics,'' AIAA Paper 91-2456, July 1991.

[13]Auweter-Kurtz, M., Gölz, T., Kurtz, H. L., and Riehle, M., ''Hydrogen Arcjet Thruster Development at the University of Stuttgart,'' International Astronautical Federation, 96-S.3.01, Oct. 1996.

[14]Kurtz, H. L., Auweter-Kurtz, M., Glocker, B., Merke, W., and Schrade, H. O., ''A 15 kW Experimental Arcjet,'' International Electric Propulsion Conf., IEPC Paper 88-107, Oct. 1988.

[15]Gölz, T., Auweter-Kurtz, M., and Kurtz, H. L., ''Development and Testing of a 100 kW Radiation-Cooled Thermal Hydrogen Arcjet Thruster,'' International Electric Propulsion Conf., IEPC Paper 93-221, Sept. 1993.

[16]Yos, J. M., ''Transport Properties of Nitrogen, Hydrogen, Oxygen and Air to 30,000 K,'' Research and Advanced Development Div., TM-63-7, Contract AF33(616)-7578, Taks 73606, AVCO Corp., Everett, VA, March 1963.

[17]Scott, C. D., ''A Nonequilibrium Model for a Moderate Pressure Hydrogen Microwave Plasma,'' NASA TM 104765, 1993.

[18]Ecker, G., ''Electrode Components of the Arc Discharge,'' *Ergebnisse der exakten Naturwissenschaften*, edited by S. Flügge und F. Trendelenburg, Vol. XXXIII, Springer–Verlag, Berlin, 1961, pp. 1–104.

[19]Myers, R., ''Energy Deposition in Low Power Coaxial Plasma Thrusters,'' Ph.D. Dissertation, Dept. of Mechanical and Aerospace Engineering, Princeton Univ., Princeton, NJ, 1989.

[20]Habiger, H., Auweter-Kurtz, M., and Kurtz, H. L., ''Electrostatic Probes for the Investigation of Arc Driven Electric Propulsion Devices,'' International Electric Propulsion Conf., IEPC Paper 93-124, Sept. 1993.

[21]Chen, S. L., and Sekiguchi, T., ''Instantaneous Direct-Display System of Plasma Parameters by Means of Triple-Probe,'' *Journal of Applied Physics*, Vol. 36, No. 8, 1965, p. 2363.

[22]Habiger, H., ''Elektrostatische Sonden und Fabry-Perot Interferometrie zur Untersuchung von lichtbogenbeheizten Plasmen für Triebwerksanwendungen und Wiedereintrittssimulation,'' Ph.D. Dissertation, Institut für Raumfahrtsysteme, Univ. of Stuttgart, Stuttgart, Germany, 1994.

[23]Habiger, H., Auweter-Kurtz, M., and Kurtz, H. L., ''Investigation of Arcjet Plumes with Fabry-Perot Interferometry,'' AIAA Paper 94-3300, June 1994.